Remote Sensing of Environment 114 (2010) 540–551

Contents lists available at ScienceDirect

Remote Sensing of Environment

journal homepage: www.elsevier.com/locate/rse

An application of the T_s–VI triangle method with enhanced edges determination for evapotranspiration estimation from MODIS data in arid and semi-arid regions: Implementation and validation

Ronglin Tang [a,b,c], Zhao-Liang Li [a,b,*], Bohui Tang [a]

[a] Institute of Geographic Sciences and Natural Resources Research, Beijing 100101, China
[b] LSIIT, Bld Sebastien Brant, BP10413, 67412 Illkirch, France
[c] Graduate University of Chinese Academy of Sciences, Beijing, 100049, China

ARTICLE INFO

Article history:
Received 19 June 2009
Received in revised form 12 October 2009
Accepted 16 October 2009

Keywords:
Evapotranspiration
MODIS
Validation
Large Aperture Scintillometer
T_s–VI triangle space

ABSTRACT

The commonly applied surface temperature–vegetation index (T_s–VI) triangle method is used to estimate regional evapotranspiration (ET) in arid and semi-arid regions. A practical algorithm based on the T_s–VI triangle method is developed to determine quantitatively the dry and wet edges of this triangle space. First, the T_s–VI triangle method is reviewed. Assumptions involved in this method are highlighted, and advantages, disadvantages and applicability are discussed. Then, an experimental use of the T_s–VI triangle method is developed and applied to several MODIS/TERRA datasets acquired during the Heihe Field Experiment from May 20th to August 21st, 2008. The sensible heat fluxes retrieved using MODIS data from a grassland located in the middle reach of Heihe river basin, Northwest China, are in good agreement with those measured from a Large Aperture Scintillometer (LAS). The Root Mean Square Error of this comparison is 25.07 W/m^2. It is shown that determination of dry and wet edges using the proposed algorithm is accurate enough at least in most cases of our study for the estimates of regional surface ET.

1. Introduction

Accurate estimates of spatially averaged evapotranspiration (ET) are of crucial importance in disciplines of hydrology, meteorology and agriculture, especially in arid and semi-arid areas where water deficiency is becoming a major constraint on economic welfare and sustainable development. Though direct measurements of turbulent heat fluxes representative of scales of hundreds and thousands of meters can be conducted by the use of either the radiosonde-based vertical profiles of regionally averaged atmospheric variables in the planetary boundary layer or the flight-path averaged turbulence statistics measured with a turbulence measurement instrument onboard an aircraft (Asanuma & Iemoto, 2007), these direct measurements can only be conducted in large scale field programs occasionally due to the high cost and discontinuity of these measurements. Remote sensing technology can provide land surface parameters such as surface temperature, albedo and vegetation indices, etc., which are indispensable to remotely sensed ET models for estimating the area averaged turbulent heat fluxes at regional scale. It is recognized as the only viable means to map regional, meso- and macro-scale patterns of ET at the earth's surface in a globally consistent and economically feasible manner.

Several remotely sensed ET models with varying complexity have been developed to map turbulent heat fluxes at various spatial scales ranging from small "point" to large "continental" scale. Inputs to remote sensing estimates of ET generally consist of surface temperature retrieved from thermal infrared channels, albedo and vegetation indices estimated from visible and near infrared spectral bands and ground-based meteorological measurements. These ET models mainly include the simplified empirical method (Jackson et al., 1977), surface energy balance based single- and dual-source models (Hatfield, 1983; Norman et al., 1995), spatial contexture information based surface temperature–vegetation indices triangular and trapezoidal methods (Jiang & Islam, 1999; Moran et al., 1994) and data assimilation techniques (Boni et al., 2001). Overviews of these models and methods have been provided by a number of authors since the 1990s (Courault et al., 2005; Glenn et al., 2007; Kairu, 1991; Kalma et al., 2008; Kustas & Norman, 1996; Li et al., 2009). Although great progress has been made on the regional remotely sensed estimate of ET with models incorporating land surface parameters retrieved quantitatively from satellite remote sensing data in the past more than 30 years, there are several related problems that have not yet been solved properly. On one hand, for lack of the validation ET data at large scale, particularly over heterogeneous surfaces with complex geographic terrains and partial vegetative covers, all developed ET

* Corresponding author. Institute of Geographic Sciences and Natural Resources Research, Beijing 100101, China.
E-mail address: lizl@igsnrr.ac.cn (Z.-L. Li).

0034-4257/$ – see front matter © 2009 Elsevier Inc. All rights reserved.
doi:10.1016/j.rse.2009.10.012

models or methods have not been rigorously validated and consequently cannot be used in confidence. On the other hand, due to the extra difficulty presented or the lack of the feasible methods to get the spatial representativeness of ground-based measurements for heterogeneous domain at large scale, such as near surface air temperature, wind speed, vapor pressure deficit and vegetation height, etc. from the limited observation networks on the Earth, most of the currently commonly applied remotely sensed ET models cannot be used operationally to map ET at large scale. In order to overcome the latter problem, attempts have been made to develop a parameterization of regional ET with only satellite derived surface parameters, such as the so-called surface temperature–vegetation index (T_s–VI) triangle method developed by Jiang and Islam (1999, 2001) and improved by Jiang and Islam (2003). The cross-sensor-platform applicability of the T_s–VI triangle method between MODIS and AVHRR data was verified by Venturini et al. (2004) and Batra et al. (2006). This type of method relies on the triangular shape formed by the scatter plot of surface temperature (T_s, or temperature difference) versus vegetation index (VI, such as Normalized Difference Vegetation Index (NDVI), Enhanced Vegetation Index (EVI), and fractional vegetation cover (F_r)) under a full range of vegetation cover and soil moisture availability within the interesting study region to estimate evaporative fraction (EF) and ET at satellite pixel resolution. The success of T_s–VI triangle method on the estimation of EF and ET depends mainly on the correct choice of the dry and wet edges in the T_s–VI triangle space. In the previous studies, the wet edge is generally identified by using the lowest observed clear pixel surface temperature in the image scene (Jiang & Islam, 2001) or air temperature (Jiang & Islam, 2003), or the average remotely sensed inland water body temperature (Jiang et al., 2009) whereas the dry edge determination cannot automatically filter the outliers and spurious dry points to guarantee the closer approaching of the observed edge to the theoretical true dry edge.

The objectives of this paper are twofold: (1) to develop an algorithm to determine quantitatively the dry and wet edges for the T_s–VI triangular space in arid and semi-arid areas where wet pixels are not generally easily identified, and (2) to validate with the in-situ ET measurements made by the Large Aperture Scintillometer (LAS) the ET derived from MODIS/TERRA products using the developed algorithm. Section 2 recalls the principle of the T_s–VI triangle method and highlights the assumptions involved in the methodological development and the advantages and disadvantages of the T_s–VI method. The implementation and application of the proposed algorithm to MODIS data are subsequently given in this section. Section 3 describes the study region and data used in the present study and gives a preliminary validation of satellite derived sensible heat flux with the field measurements made by the LAS. Finally, the conclusion is given in Section 4.

2. Methodology

2.1. Review of T_s–VI method

Spatial contextual information of T_s versus VI triangle relationship, first proposed by Goward et al. (1985), has been applied successfully to study soil moisture water content, land use and land cover change and drought monitoring (Carlson et al., 1995; Hassan et al., 2007; Lambin and Ehrlich, 1996; Nemani et al., 1993; Price, 1990; Sun & Kafatos, 2007; Sun et al., 2008). Such a triangle is characterized by two physical bounds: the upper decreasing dry and lower nearly horizontal wet edges (see Fig. 1 as an example). These edges respectively represent two limiting cases of soil moisture and evaporative fraction for each VI value (i.e., the unavailability of soil moisture at the dry edge and the potential ET at the wet edge).

T_s–VI triangle (see Fig. 1) method applied in this paper is originated from the parameterization of Jiang and Islam (1999), in which a simplified Priestley–Taylor formulation (Priestley & Taylor, 1972) with fully remotely sensed data is utilized to estimate regional ET and EF by interpreting the scatter plot constructed from remotely sensed T_s and VI under conditions of full ranges of soil moisture availability and vegetation cover. This approach is based on an extension of Priestley–Taylor's equation and the existence of physically meaningful relationship between evaporative fraction and remotely detectable surface characteristic parameters (T_s, NDVI, soil moisture, vegetation fraction). The mathematical expression of latent heat flux (LE) is taken as follows (Jiang & Islam, 1999):

$$LE = \phi\left[(R_n - G)\frac{\Delta}{\Delta+\gamma}\right] \quad (1)$$

where ϕ is a combined-effect parameter which accounts for aerodynamic resistance (dimensionless), R_n is surface net radiation (W/m^2), G is soil heat flux (W/m^2), Δ is slope of saturated vapor pressure versus air temperature (kPa/°C), γ is Psychrometric constant (kPa/°C).

Parameter ϕ is derived using a two-step interpolation scheme from the dry and wet edges in the T_s–VI triangular space. Detailed description will be given in Section 2.3. As shown by Jiang and Islam (1999), Jiang et al. (2004) and Wang et al. (2006), the sensitivity of $\Delta/(\Delta+\gamma)$ on the variation of temperature is very small, air temperature (T_a) required in Eq. (1) to calculate $\Delta/(\Delta+\gamma)$ can be obtained either by a linear regression between T_s and T_s–T_a or by using mean surface temperature or mean water surface temperature as a surrogate (Jiang & Islam, 1999; Venturini et al., 2004). In this work, taking into account the small sensitivity of $\Delta/(\Delta+\gamma)$ and the correlation of T_s with air temperature, remotely sensed T_s will be used to estimate the parameter Δ instead of the use of air temperature.

It should be noted that all quantities involved in the right hand side of Eq. (1) can be derived from remotely sensed data alone and according to the definition of EF, EF can be directly estimated from Eq. (1) as:

$$EF = \phi\frac{\Delta}{\Delta+\gamma}. \quad (2)$$

Although parameter ϕ in Eq. (1) looks apparently the same as α in Priestley–Taylor's equation, there is a distinct difference in the physical meaning between these two parameters. In Priestley–Taylor's equation, α is generally interpreted as the ratio of actual

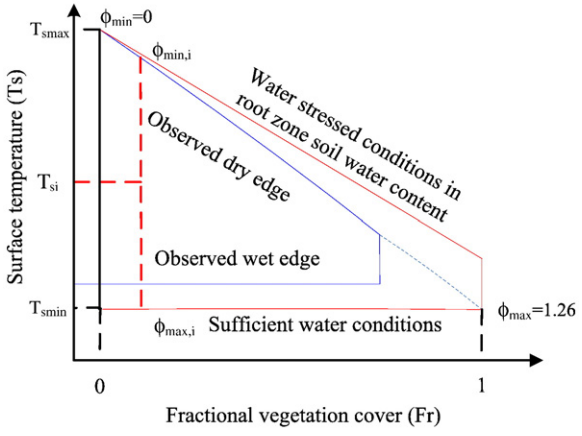

Fig. 1. Schematic diagram of the conceptual surface temperature–vegetation fraction (T_s–F_r) triangular space (upper and lower blue solid lines respectively represent observed dry and wet edges from remotely sensed data; upper and lower red solid lines respectively represent true dry edge with water stressed conditions in root zone soil water for different vegetation covers and true wet edge with sufficient water conditions).

evaporation to the equilibrium evaporation and a series of paper has demonstrated this parameter with a good approximate to be 1.26 (Crago & Brutsaert, 1992; Jiang & Islam, 2001). Priestley–Taylor's equation is generally applicable for wet surfaces whereas Eq. (1) holds true for a wide range of surface evaporative conditions with ϕ varying from 0 to $(\Delta+\gamma)/\Delta$ when significant advection and convection are absent. Jiang and Islam (1999) have found the upper bound of derived ϕ (corresponding to the wet edge in the T_s–VI triangle space) for each NDVI value is very closed to 1.26.

Several modified versions of T_s–VI triangle method have been applied with remote sensing data derived from MODIS and AVHRR sensors to estimate the regional EF and ET mainly over the Southern Great Plain (SGP) in the United States. In the work of Stisen et al. (2008), MSG-SEVIRI derived temperature difference dT_s was plotted against NDVI to establish the triangular feature space, in which the minimum ϕ along the dry edge was interpolated non-linearly with NDVI between global minima and maxima while ϕ value for intermediate pixels was interpolated linearly between minimum and maximum ϕ within each NDVI interval. Carlson (2007) showed how temporal trajectories of points described the land use change in a universal (scaled T_s–VI) triangle. Wang et al. (2006) combined advantages of thermal inertial method and T_s–NDVI spatial variation method to develop a modified day–night T_s difference–NDVI triangle using data from MODIS Terra and Aqua land surface products to estimate the regional EF and analysis was performed with data collected from energy balance Bowen ratio system at 11 enhanced facilities over SGP from April 2001 to May 2005. Batra et al. (2006), Venturini et al. (2004) and Jiang and Islam (2001, 2003) have respectively established their own T_s–NDVI triangles to demonstrate the applicability and operationality of this simple scheme in the estimation of regional ET and EF over larger areas.

Assumptions involved in the T_s–VI triangle method are that 1) variations in surface temperature for given vegetation index (VI) are primarily caused not by differences in the atmospheric forcing but the different soil moisture availabilities, and 2) sensitivity of T_s to soil and canopy differs and canopy temperature is insensitive to soil moisture change at surface/deep layer.

Advantages of T_s–VI triangle method over the residual method of surface energy balance for ET estimation are that 1) absolute high accuracy in remotely T_s retrieval and atmospheric correction are not indispensable, 2) complex parameterization of aerodynamic resistance and uncertainty originated from replacement of aerodynamic temperature by remotely sensed T_s is bypassed, 3) no ground-based near surface measurements are needed other than remotely sensed T_s and VI, 4) a direct calculation of EF, defined as the ratio of latent heat flux to surface available energy, can be obtained without resort to surface energy balance, and 5) estimations of EF and R_n are independent from each other by this method. Therefore, the overall errors in ET can be traced back to EF and R_n separately. There are some other methods making the estimation of EF and R_n dependent on each other (among others, Bastiaanssen (2000); Norman et al. (1995)), thus making it impossible to trace errors separately. Limitations of T_s–VI triangle mainly lie in a bit subjective determination of both dry and wet edges and a large number of pixels required over a flat area with a wide range of soil moisture and fractional vegetation cover.

2.2. Automatic edges determination algorithm for the T_s–VI triangle

Taking into account that NDVI is just a surface greenness parameter and dependent on spatial resolution of remote sensors (Price, 1990), the commonly employed NDVI in the construction of T_s–VI triangle space will be replaced in this paper by the fraction of vegetation (F_r) which seems to be more representative of the relative proportionality between soil and vegetation within the pixel. A theoretical interpretation of the conceptual T_s–F_r triangle (trapezoid) is given in Fig. 1. Overall, the dry edge and wet edge form two physical limits of the T_s–F_r triangle (trapezoid). For a given F_r (F_{ri}), surface temperature (T_s) increases progressively as a result of water stress in the surface soil from minimum value ($T_{smin,i}$) at wet edge to maximum value ($T_{smax,i}$) at dry edge whereas EF decreases from maximum ($EF_{max,i}$) to minimum ($EF_{min,i}$) values correspondingly. Specifically, pixels at the (true) wet edge are regarded to evaporate (transpire) potentially with $EF = EF_{max,i} = 1$ while at (true) dry edge ET mainly comes from the transpiration of vegetation from the root zone water. EF at dry edge ($EF_{min,i}$) varies from 0 at bare soil to 1 at full vegetation cover when root zone soil water is not stressed. Jiang and Islam (2003) assumed a linear variation of EF with F_r at the dry edge between ($EF_{min,0} = 0$, $F_r = 0$) and ($EF_{min,1} = 1$, $F_r = 1$). Stisen et al. (2008) proposed a quadratic function of NDVI for determination of $\phi_{min,i}$ at dry edge, equivalent to a linear function between EF and F_r with consideration of small sensitivity of $\Delta/(\Delta+\gamma)$ to air temperature. Under water stress conditions in the root zone soil water, surface temperature at dry edge for a (partially or fully) vegetated surface will be higher. Jiang and Islam (2003) introduced a correction parameter η (varying from 0 to 1) to account for the water stress conditions at dry edge where EF is equal to $\eta EF_{min,i}$. Under extreme circumstances, $\eta = 1$ means no water stress in the root zone soil water while $\eta = 0$ indicates no evaporation at all at dry edge even for the vegetated surface, which seems to violate the observations and does not make sense as to the physiological growth of the green vegetation. Although the exact relationship between $EF_{min,i}$ ($\phi_{min,i}$) and F_r has not been explored explicitly, it appears that $EF_{min,i}$ ($\phi_{min,i}$) as a linear function of F_r can give satisfactory results when no water stress conditions in the root zone soil water occur at dry edge. As for wet edge determination, previous works (Carlson, 2007; Jiang & Islam, 1999) have recommended taking the surface temperature of a water body and/or a well-irrigated agricultural field as the temperature of wet edge with potential ET. In addition, for a given F_r, Jiang et al. (2004) theoretically verified the linear variation of EF with surface temperature (or temperature difference) from the bulk transfer equation for sensible heat flux and deduced the error bounds of EF in the T_s–VI triangle in a semi-empirical manner.

To estimate pixel by pixel ET and EF using Eqs. (1) and (2), both dry and wet edges in the T_s–F_r space have to be first determined. In arid and semi-arid areas, for a given vegetation cover, spatial pixels with high surface temperature and low EF are more readily detectable by satellite remote sensors than potentially evaporating pixels (such as inland water body surface, fully vegetated surface) which may hardly exist. For these areas, the observed dry edge from the satellite remote sensors can represent the true dry edge with water stress correction parameter $\eta = 1$ whereas surface temperatures at observed wet edge may be higher than those at true wet edge (sufficient water conditions). Therefore, in arid and semi-arid regions, directly applying the observed wet edge as the true wet edge in T_s–VI triangle space will result in overestimates of EF and ET. It should be noted that even if pixels under different vegetation cover conditions evaporate (transpire) potentially for given similar atmospheric forcing, there will be temperature difference for these pixels (i.e. surface temperature of a bare soil with potential evaporation may be lower than that of fully vegetation cover pixel with potential transpiration). However, this difference should be small and is relatively unimportant in the estimates of EF and ET. Assuming the wet edge to be a constant temperature regardless of F_r and equal to the temperature of dry edge at $F_r = 1$ in the T_s–F_r space should not incur large error in the resultant EF and ET estimates as demonstrated in Section 3.

With the assumption that surface temperature at the dry edge is a linear function of F_r and the true wet edge is a constant value in T_s–VI triangle space, theoretically, the dry and wet edges can be both determined once the highest surface temperature ($EF_{min,0} = 0$) at $F_r = 0$ and surface temperature at water body surface or fully vegetated surface are known. However, these two land surface types cannot be easily identified or may not exist at all in most arid and semi-arid areas, an automatic and practical algorithm thereby needs to be developed to determine the dry and wet edges in the triangular space for these areas (see Fig. 2).

In this paper, an iterative process is proposed to determine automatically the two edges in the T_s–F_r triangle space (see Fig. 2). This process can automatically filter the spurious dry points and is more robustly resistant to the outliers. Below is the description of each step in the proposed algorithm.

(i) Dividing the range of F_r in the T_s–F_r triangle space into M intervals evenly ($M \leqq 20$ is recommended) and then dividing each interval into N subintervals ($N \geqq 5$ is recommended);
(ii) For a given interval, finding and saving the maximum temperature within each subinterval;
(iii) The average value (T_{aver}) and standard deviation (δ) of the N maximum surface temperatures for N subintervals of this given interval are computed as an initial state.
(iv) If the maximum surface temperature of each subinterval of this given interval is less than T_{aver}–δ, this subinterval is discarded in the following steps.
(v) The new average value (T_{aver}) and standard deviation (δ) of the maximum surface temperatures of the remaining subintervals after step (iv) are recomputed.
(vi) If the number of remaining subintervals in the given interval is greater than a given threshold value and δ is larger than a given threshold value, go back to step (iv) and repeat the steps (iv)–(vi), otherwise go to step (vii).
(vii) Taking T_{aver} as the maximum surface temperature of this given interval and going back to step (ii) until all the maximum surface temperatures are found for all M intervals.
(viii) A linear regression between the maximum surface temperature within each F_r interval and F_r value is performed and the Root Mean Square Error (RMSE) is computed.
(ix) If the maximum surface temperature for a given interval is 2 times RMSE or more less than the temperature value in the regressed line, this interval will be discarded and the program will go back to step (viii) until the minimum number of intervals is reached or no interval can be further discarded.
(x) A final linear regression is performed to obtain the dry edge:

$$T_{\max,i} = a + bF_r, \tag{3}$$

with the two extreme points ($T_{max,i} = T_{smax}$ at $F_r = 0$ and $T_{max,i} = T_{smin}$ at $F_r = 1$) depicted in Fig. 1, one gets:

$$a = T_{s\max} \text{ and } b = T_{s\min} - T_{s\max}.$$

As mentioned above, this work assumes that the wet edge is the line with a constant surface temperature which is equal to that of dry edge at $F_r = 1$, i.e.

$$T_{\min,i} = a + b = T_{s\min}.$$

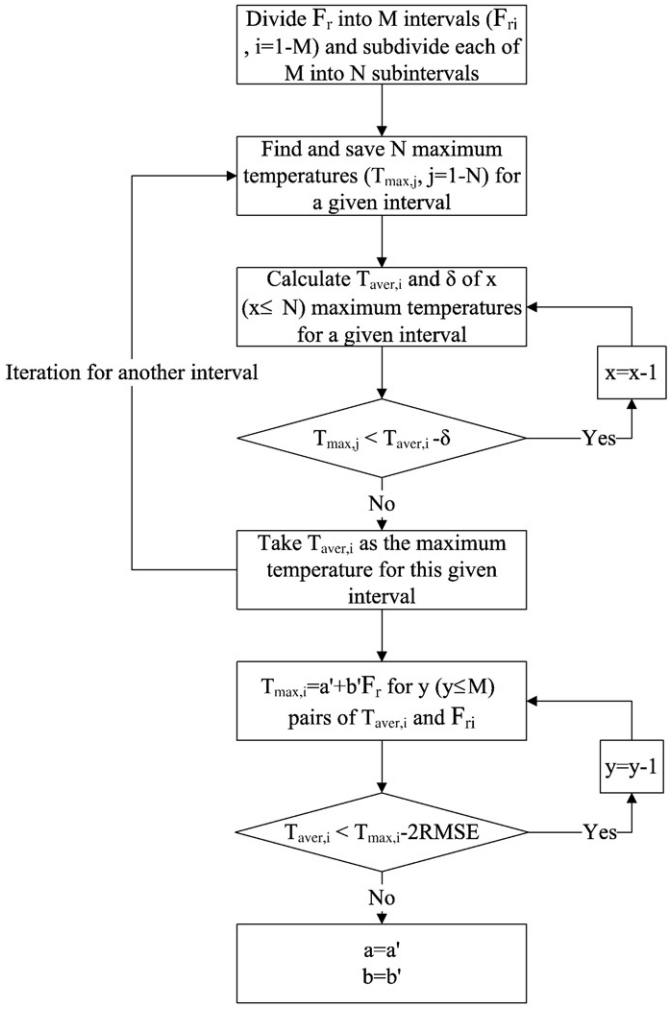

Fig. 2. Flow chart of the algorithm of our proposed dry edge determination in the T_s–F_r triangular space.

2.3. Applications to MODIS data

To apply the above T_s–F_r triangle method to MODIS data, several steps are needed to be performed as shown in Fig. 3. The input MODIS data and products are MODIS land surface temperature/emissivity products (MOD11) and NDVI (MOD13) from the Land Processes Distributed Active Archive Center (LP DAAC) (http://lpdaac.usgs.gov/), together with MODIS Calibrated Radiances (MOD021KM), MODIS Geolocation (MOD03) and MODIS Precipitable Water (MOD05_L2) products from the LAADS (Level 1 and Atmosphere Archive and Distribution System) web (http://ladsweb.nascom.nasa.gov). The output datasets consist of the derived R_n, G, EF and ET. Below is the description of each step involved in the algorithm.

2.3.1. Downloading MODIS land surface temperature/emissivity and NDVI products, MODIS Calibrated Radiances and Geolocation products, as well as MODIS Atmospheric Precipitable Water product from the MODIS data and products centers

In order to establish the T_s–F_r triangle space, MODIS land surface temperature/emissivity product (MOD11A1 and MOD11_L2) and NDVI product (MOD13A2) are needed to be first downloaded from the Land Processes Distributed Active Archive Center (LP DAAC) (https://lpdaac.usgs.gov/). In addition, MODIS Calibrated Radiances (MOD021KM), Geolocation (MOD03) and Atmospheric Precipitable Water (MOD05_L2) products are used to estimate the surface net radiation R_n and they can be downloaded from the LAADS (Level 1 and Atmosphere Archive and Distribution System) web (http://ladsweb.nascom.nasa.gov).

2.3.2. Screening out the pixels contaminated by cloud and also the pixels with surface elevation far apart from the average of surface elevation in the study area

Having successfully downloaded all MODIS data and products, some preliminary processing are needed to be performed using Modis Reprojection Tool (MRT) and MODIS Swath Reprojection Tool (MRTSwath) so that all data and products are well georeferenced and subset corresponding to the study area is easily accomplished. As well known, the cloud affects significantly the satellite-derived T_s, pixel contaminated by cloud in the study area are therefore screened

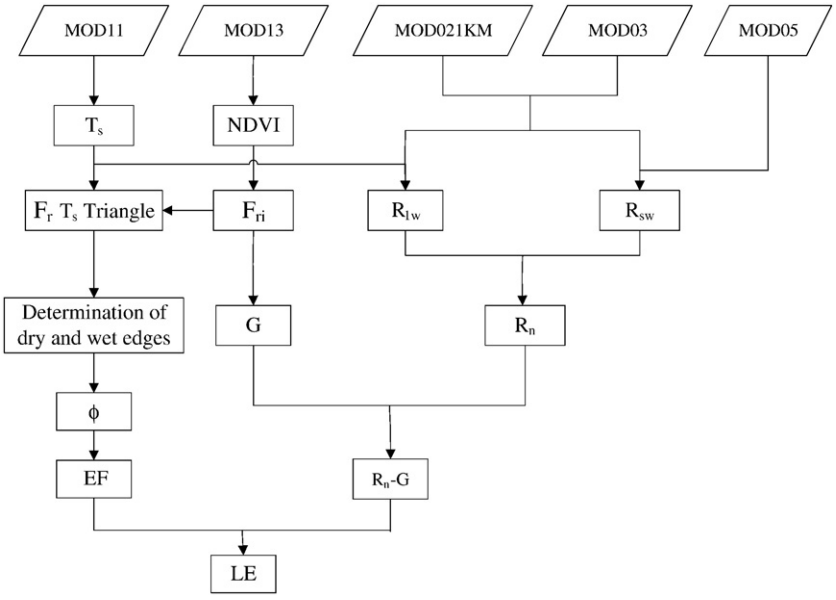

Fig. 3. Flow chart of the proposed algorithm to estimate the regional surface net radiation, soil heat flux, evaporative fraction and latent heat flux from MODIS data.

out. Moreover, as T_s change in the T_s–VI space is assumed to be primarily caused by surface evaporative cooling effect instead of the elevation variation, all pixels in the T_s–F_r triangle space should have about the same surface elevation, thus pixels having much higher or lower surface elevation with respect to the average of elevation in the study area are also removed out.

It is worth noting that the subset selected should be as large as possible so that the large ranges of both soil moisture availability and vegetative coverage could be found in the study area.

2.3.3. Estimating the fraction of vegetation (F_r) for each pixel in the study area

As stated in Section 2.2, to construct the T_s–VI triangle space, F_r is used in this work to replace the NDVI. Pixel by pixel F_r is therefore estimated from MODIS NDVI product using the formula proposed by Carlson and Ripley (1997):

$$F_r = \left(\frac{NDVI - NDVI_{min}}{NDVI_{max} - NDVI_{min}}\right)^2 \quad (4)$$

where $NDVI_{min}$ and $NDVI_{max}$ are respectively the minimum NDVI corresponding to bare soil and the maximum NDVI corresponding to fully vegetated surface. They are assigned respectively to be 0.2 and 0.86 in this work as done by Prihodko and Goward (1997).

Noting that estimation of F_r using NDVI instead of using the newly MODIS developed Enhanced Vegetation Index (EVI) product is due to the fact that, to our knowledge, there is no formula available nowadays to relate F_r to EVI.

2.3.4. Constructing the T_s–F_r triangle space

Knowing T_s and F_r, a plot of T_s against F_r (T_s represents the ordinate axis and F_r represents the abscissa) for all remained pixels after the step 2.3.2 in the study area is used to construct the T_s–F_r triangle feature space bounded with an upper decreasing envelope and a lower nearly horizontal envelope.

2.3.5. Determining automatically the dry and wet edges in the T_s–F_r triangle space

After having plotted the pixels in our study region in two-dimensional space (F_r, T_s), one needs to determine carefully the dry and wet edges in this T_s–F_r space using the algorithm described in Section 2.2 because accurate determination of these two edges has direct impact on the accuracy of the derived EF and turbulent heat fluxes.

2.3.6. Calculating pixel by pixel the combined-effect parameter ϕ

After having determined the dry and wet edges at step (2.3.5), as depicted in Fig. 1, the value of ϕ corresponding to the driest bare soil pixel (at the position $F_r = 0$ and maximum surface temperature T_{smax} in the dry edge line) is set to 0 (denoted as $\phi_{min} = 0$ at pixel ($F_r = 0$, T_{smax})) and the value of ϕ at the position $F_r = 1$ and the minimum surface temperature T_{smin} in the dry edge line is set to 1.26 (denoted as $\phi_{max} = 1.26$ at ($F_r = 1$, T_{smin})). A two-step linear interpolation is then used to get the ϕ value for the pixel i (F_{ri},T_{si}) in the T_s–F_r triangle space — 1) determining ϕ_{min} value in the dry edge line for the pixel i ($\phi_{min,i}$) by assuming that $\phi_{min,i}$ varies linearly with F_r between $\phi_{min} = 0$ at ($F_r = 0$, T_{smax}) and $\phi_{max} = 1.26$ at ($F_r = 1$, T_{smin}), and determining ϕ_{max} value for the pixel i ($\phi_{max,i}$) in the wet edge line by assuming that $\phi_{max,i}$ is constant in the wet edge line, i.e. $\phi_{max,i} = \phi_{max} = 1.26$ as the wet edge line is defined as $T_s = T_{smin}$; and 2) determining ϕ value for the pixel i, ϕ_i, by assuming that for given F_r, ϕ increases linearly with the decrease of T_s between $\phi_{min,i}$ and $\phi_{max,i}$. According to the above-mentioned two-step interpolation scheme (see Fig. 1), the lower limiting value of ϕ for any F_r ($\phi_{min,i}$) in the dry edge can be first derived by a linear interpolation between $\phi_{min} = 0$ at $F_r = 0$ and $\phi_{max} = 1.26$ at $F_r = 1$, namely:

$$\phi_{min,i} = 1.26F_r \quad (5)$$

then for the pixel (F_r, T_{si}) in the T_s–F_r triangle, ϕ is once again assumed to increase linearly with the decrease of T_s between $\phi_{min,i}$ and $\phi_{max,i}$ for a given F_r, i.e.,

$$\phi = \frac{T_{max,i} - T_{si}}{T_{max,i} - T_{min,i}}(\phi_{max,i} - \phi_{min,i}) + \phi_{min,i} \quad (6)$$

in which

$$T_{max,i} = T_{s\,max} + F_r(T_{s\,min} - T_{s\,max})$$

$$T_{min,i} = T_{s\,min}$$

$$\phi_{max,i} = \phi_{max} = 1.26.$$

2.3.7. Retrieving evaporative fraction (EF) from the combined-effect parameter ϕ

Once the combined-effect parameter ϕ is obtained, the evaporative fraction (EF) can be estimated using Eq. (2) with Δ calculated with T_s instead of T_a.

2.4. Estimation of net radiation

Surface net radiation (R_n) is defined as the sum of surface net shortwave radiation (R_{sw}) and net longwave radiation (R_{lw}). In this work, a parameterization of R_{sw} fully based on MODIS products proposed by Tang et al. (2006) is used, namely:

$$R_{sw} = \frac{E_0 \cos\theta_s}{D^2}(\alpha' - \beta' r), \tag{7}$$

with

$$\alpha' = 1 - a_1/\mu - a_2/\mu^x - (1-\exp(-\mu))(a_3 + a_4 w^y)/\mu$$

$$\beta' = 1 + a_5 + a_6 \ln\mu + a_7 w^z$$

$$r = b_0 + \sum_{i=1}^{7} b_i \rho_i$$

where E_0 is solar irradiance at Top Of Atmosphere (TOA), θ_s is the solar zenith angle extracted from MODIS Geolocation product (MOD03), D is the earth–sun distance in astronomical unit, r is the broadband albedo at TOA, μ is the cosine of solar zenith angle, a_1–a_7, x, y, z are constants for various types of surfaces (Land, Ocean, and Snow/Ice) and predefined in table 4 of Tang et al. (2006), w is the precipitable water extracted from MODIS Atmospheric Precipitable Water product (MOD05_L2), b_0–b_7 are the coefficients depending on the view zenith angle and the solar zenith angle both retrieved from MOD03, ρ_i is the TOA narrowband reflectance measured by MODIS band i (i=1–7) retrieved from MODIS Calibrated Radiances product (MOD021KM).

Similar to the calculation of surface net shortwave radiation, Tang and Li (2008) further proposed a scheme to directly estimate the downward longwave radiation (L_d) from only radiances measured at the TOA by six MODIS thermal infrared channels—28, 29, 31, 33, 34 and 36 and surface emitted radiation from the MODIS land surface temperature/emissivity products (MOD11) using the following formulae:

$$L_d = c_0 + c_1 \times M_{29} + c_2 \times M_{34} + c_3 \times M_{33} + c_4 \times M_{36} + c_5 \times M_{28} + c_6 \times M_{31} \tag{8}$$

$$R_{lw} = \varepsilon_s L_d - 5.67 \times 10^{-8} \varepsilon_s T_s^4 \tag{9}$$

$$\varepsilon_s = 0.273 + 1.778\varepsilon_{31} - 1.807\varepsilon_{31}\varepsilon_{32} - 1.037\varepsilon_{32} + 1.774\varepsilon_{32}^2 \tag{10}$$

where c_i (i=0–6) are coefficients depending on the view zenith angle and surface altitude both extracted from MOD03, M is the TOA radiance measured by the MODIS thermal infrared channel extracted from MOD021KM and the number in the subscript indicates the thermal channel of MODIS sensor, ε_s is the surface emissivity, T_s is surface temperature (K), ε_{31} and ε_{32} are respectively surface emissivity in MODIS channels 31 and 32 retrieved with T_s from MOD11.

Readers are recommended to refer to Tang et al. (2006) and Tang and Li (2008) for detailed information about these algorithms of retrieving surface net radiation from MODIS products.

2.5. Estimation of soil heat flux

Soil heat flux (G) is the heat energy used to cool or warm the subsurface soil. It is theoretically proportional to the thermal conductivity and vertical temperature gradient in the subsurface soil. Since it is impossible to measure G at regional scale at ground, a great number of papers have been devoted to estimating soil heat flux indirectly from certain land surface parameters retrieved from satellite data such as T_s, NDVI, LAI, Albedo and F_r (Allen et al., 2007; Bastiaanssen, 2000; Choudhury, 1989). In this work, the ratio of G to R_n (Γ) is assumed to be linearly decreasing from the dry bare soil to full vegetation cover with the increase of F_r as proposed by Su (2002):

$$\Gamma = G/R_n = \Gamma_v + (1-F_r)(\Gamma_s - \Gamma_v) \tag{11}$$

where Γ_v and Γ_s are respectively fractions for the full vegetation cover and dry bare soil. According to the in-situ point measurements, $\Gamma = G/R_n$ ranges from 0.05 for full vegetative cover (F_r=1) to a maximum of 0.3 to 0.5 for dry bare soil (F_r=0) depending on the different types of soils (Daughtry et al., 1990; Li & Lyons, 1999). In this work, Γ_v=0.05 and Γ_s=0.4 (average of 0.3 and 0.5) are assumed.

Knowing the surface net radiation (R_n), soil heat flux (G) and EF, the ET can be straightforward derived using Eq. (1).

3. Results and validation

3.1. Study area

A large and intensive field experiment was conducted in Heihe river basin from May 20th to August 21st 2008. This experiment aimed to better understand the hydrological and related ecological processes at watershed scale and to promote the quantitative remote sensing in watershed science related studies. In the experiment, a very dense network of stations, including automatic meteorological stations, hydrological stations, rain gauges, rainfall radar and flux towers, etc., has been installed to collect atmospheric and ground data. For further information about the Heihe field experiment, readers are referred to Li et al. (2008). Heihe river basin is influenced by East Asian Monsoon climate and has heterogeneous distribution of precipitation during the year. Mean annual rainfall in this basin is approximately 174 mm and more than 73% of annual rainfall occurs during the rainfall season from June to September. Our study area is located in the middle reach of Heihe river basin, Northwest China, with the climate being arid in temperate zone and total area about 38,000 km^2 (the latitude ranging from 38.7°N to 39.8°N and longitude being 98.5°–102°E). Fig. 4(a) shows a yearly IGBP land cover classification map in 2004 over the study area derived from the MODIS land cover type (MOD12Q1). Surface elevation in most areas is approximately 1200–1600 m above sea level. A mountain with elevation of about 3000 m lies in the southwestern part of the study area. The zone where our LAS instrument was set up is sparsely vegetated surfaces with short grass and agricultural crops as shown in Fig. 4(b).

3.2. Large Aperture Scintillometer and meteorological data

LAS operations were continually conducted during the Heihe field experiment over flat grassland along northeast–southwest direction from May 20th to August 21st, 2008. Calibration of LAS measurements was made with observations from an Eddy Correlation system (later dismantled for unknown reasons) nearby the transmitter of the LAS during the first several days after LAS was installed. Location of the LAS is indicated by the blue filled rectangle in Fig. 4(a) and the zoomed-in map of LAS installed area is given in the image of Fig. 4(b). Length path between transmitter and receiver of LAS is 1550 m and the surface elevations of the sites of transmitter and receiver are respectively 1384 m and 1395 m. Land covers between transmitter and receiver of LAS are mainly composed of short grass, clover, and reed. Surface of reedy patch (about 0.25 km^2) remains permanently wet due to the standing water and shallow groundwater tables in this area. The combination of wet surface types with the arid climate here

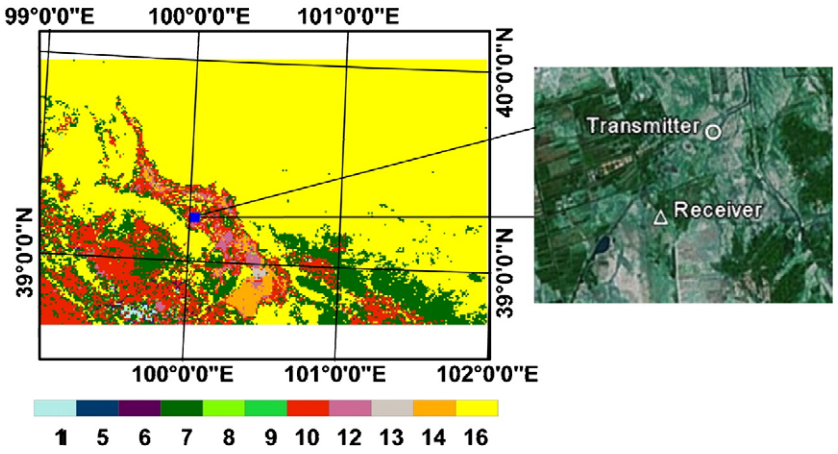

Fig. 4. A quick view of study area and location of the LAS instrument. ((a) A yearly IGBP land cover classification map in 2004 from MOD12Q1. 0 = water, 1 = evergreen needleleaf forest, 2 = evergreen broadleaf forest, 3 = deciduous needleleaf forest, 4 = deciduous broadleaf forest, 5 = mixed forests, 6 = closed shrubland, 7 = open shrublands, 8 = woody savannas, 9 = savannas, 10 = grasslands, 11 = permanent wetlands, 12 = croplands, 13 = urban and built-up, 14 = cropland/natural vegetation mosaic, 15 = snow and ice, 16 = barren or sparsely vegetated. (b) The zoomed-in map of the LAS instrument site).

has induced a thin saline–alkaline soil surface where short grass and clover are distributed. Several temporally discrete measurements of soil water content at depths of 5–100 cm (soil type: loam) by gravimetric method in the short grass and clover sampling area shows volumetric soil water content during the LAS operation period varied from about 15% to 45%. In most cases, the volumetric soil water content was greater than 30%. Both the transmitter and receiver were installed on two tripods fixed with two towers at the heights about 9.25 and 9.1 m respectively above ground. Power was supplied by two different solar power panels and a battery. 10-min interval values of both UC_n^2 (function of the logarithm of structure parameter of the refractive index of air with 10 as the base) and signal strength, and the variance of UC_n^2 were stored in a built-in data logger.

Two meteorological stations surrounding the transmitter of LAS, namely a station jointly set up by China and Japan (hereinafter referred to as "China–Japan station") and an automatically recorded station (hereinafter referred to as "automatic station"), were deployed respectively before and during the period of LAS measurements. Both stations were equipped with a set of standard meteorological instruments to measure air temperature, wind speed and direction, relative humidity and atmospheric pressure, etc. The meteorological measurements were made respectively at 10 m for China–Japan station and at 1.5 m for the automatic station and were recorded every ten minutes as that of LAS.

Post-processing of the LAS-measured data is performed with the support of WINLAS software developed by Kipp and Zonen to calculate sensible heat fluxes representative of spatially averaged values. Inputs to the WINLAS mainly include LAS measurements of UC_n^2 and signal strength and additional meteorological observations of wind speed, atmospheric pressure, air temperature, relative humidity and Bowen ratio, surface roughness and displacement height, length and height of path. Monin–Obukhov Similarity Theory (MOST) is applied in WINLAS software to derive sensible heat flux from the LAS measurement and other additional data. At near infrared wavelength of 880 nm, the observed scintillations are primarily caused by turbulent temperature fluctuations. In this case, the relationship between the structure parameter of temperature (C_T^2) and the structure parameter of the refractive index of air (C_n^2) can be simplified as:

$$C_n^2 \approx \left(\frac{-0.78\cdot 10^{-6}P}{T_a^2}\right)^2 C_T^2\left(1+\frac{0.03}{\beta}\right)^2, \tag{12}$$

where P is atmospheric pressure (P_a), β is the Bowen ratio. The last term in the right hand of equation (after C_T^2) is a correction for humidity related scintillations. For unstable conditions, sensible heat flux is related to C_T^2 based on MOST (Wyngaard et al., 1971) with the following equation:

$$\frac{C_T^2(z_{LAS}-d)^{2/3}}{T_*^2} = 4.9\left(1-6.1\frac{z_{LAS}-d}{L_{MO}}\right)^{-2/3}, \tag{13}$$

where z_{LAS} is the height of the LAS above the surface (m), d is the zero-displacement height (m), T_* is temperature scale (dimensionless), L_{MO} is the Obukhov length (m).

As Bowen ratio (β) is not a constant during the period of LAS operations and no other Bowen ratio data can be acquired, this work attempts to apply the average values of few-day Eddy Correlation system-measured data derived at the beginning of LAS operation to the calculation of LAS-measured sensible heat flux for whole period of the experiment. Since there is no remarkable variation visually in the vegetation height during the period of operation of LAS, surface roughness and displacement height are respectively assigned to the fixed values using rule of thumb assumptions with $z_{0m} = 0.1$ m and $d = 0.5$ m for simplicity and operational convenience.

The uncertainty of LAS-measured sensible heat flux from inputs to WINLAS software is evaluated based on Gaussian Error Propagation, which can be expressed in first order accuracy as standard deviation σ. For a function F with n independent variables x ($x_i = 1$ to n), the uncertainty (σ) can be estimated as:

$$\sigma^2 = \sum_{i=1}^{n}\left(\frac{\partial F}{\partial x_i}\right)^2 \sigma_{x_i}^2, \tag{14}$$

where σ_{xi} is the uncertainty in x_i.

Following the work of Marx et al. (2008) and taking into account the actual situations and conditions in our experiment, Table 1 lists the tolerances of the ten variables which influence the accuracy of LAS-measured sensible heat flux (H). Assuming these ten variables are independent (Marx et al., 2008) and under the normal conditions at the time of MODIS data used in this study, as predicted by Eq. (14) with the uncertainties of variables listed in Table 1, contribution of each variable to the uncertainty of LAS-measured H is given in the fourth column of Table 1 and overall uncertainty of LAS-measured H is about 9.2 W/m^2. From this table, one can see that Bowen ratio has large impact on the LAS-measured H (8.1 W/m^2) while measurement uncertainties of meteorological variables have negligible impacts in our study.

As two meteorological stations operated near our LAS instrument, one is the China–Japan station which was in operation during the

Table 1
Tolerances used to evaluate the uncertainty in LAS-measured H.

Quantity (x)	Unit	Assumed relative uncertainty (%)	Induced uncertainty of H (W/m^2)
Air temperature	°C	±1	0.16
Wind speed	m/s	±1	0.38
Atmospheric pressure	hPa	±1	0.61
Relative humidity	–	±10	0.10
Bowen ratio	–	−75	8.13
Roughness length	m	±10	0.99
Path length	m	±1	2.72
Height of wind speed measurements	m	±1	0.07
Path height	m	±1	1.10
UC_n^2	V	±1	2.84

whole period of the field experiment and another is the automatic station operated only from May 26th to July 16th. Since the LAS instrument cannot measure directly the sensible heat flux (H), H can only be derived from LAS-measured data in combination with Bowen ratio, surface roughness length, displacement height and the atmospheric parameters/variables measured at meteorological station as described above. Fig. 5 shows good agreement between MODIS overpass-time LAS-measured H with atmospheric parameters/variables collected respectively from both stations. In this figure, H estimated using automatic station seems slightly larger than that derived using China–Japan station at higher H values. The RMSE between them is 9.41 W/m^2 and R^2 is 0.962. This good agreement demonstrates the consistency of LAS-measured H with meteorological data collected respectively from China–Japan station and automatic station. Therefore, in the following, only H derived from LAS data using atmospheric parameters/variables measured at the China–Japan station will be compared with H derived from MODIS data using the T_s–F_r triangle method.

In order to evaluate the reliability of inferred LAS-measured H, Fig. 6 shows a comparison of H derived respectively from Eddy Correlation system (EC) and LAS measurements on May 20th from 8 h to 18 h. Relatively good agreement in the morning is observed between LAS-measured and EC-measured H though EC-measured H is slightly higher than that deduced from LAS measurements. Larger differences observed in the afternoon may result from 1) the strong turbulent mixing of heat in the planetary boundary layer, 2) the surface heterogeneity between LAS and EC sites, and 3) the inconsistent source areas of those two H measurements. Fluxes

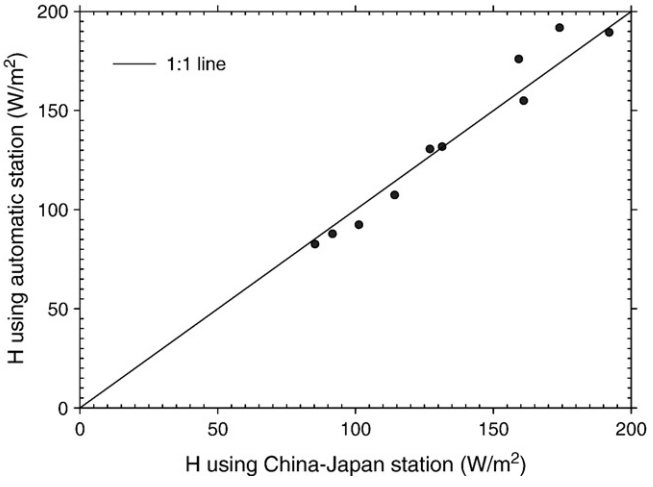

Fig. 5. Comparison of MODIS overpass-time LAS-measured sensible heat fluxes calculated respectively using measurements at China–Japan station and automatic station.

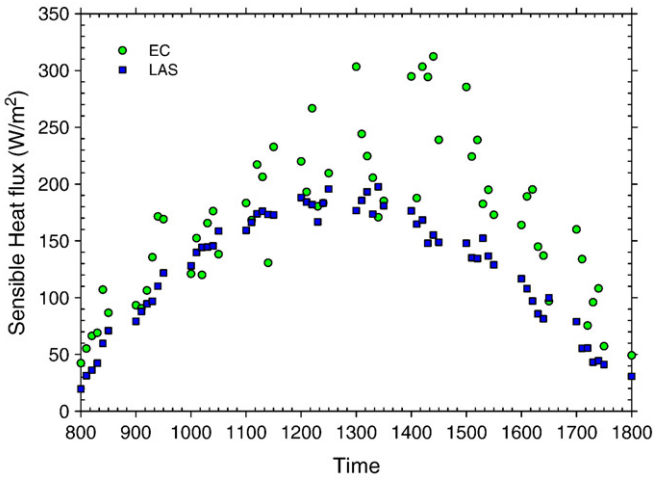

Fig. 6. Comparison of sensible heat fluxes measured on May 20th by LAS and Eddy Correlation system (time 800 means 8 h).

obtained from EC measurements are only representative of a relatively small area (on the order of 10^2 m^2) around the EC site while LAS is capable of measuring temporally continuous H over path lengths of few kilometers (the only meaningful comparison between LAS and EC can be made when heterogeneity within the footprints and differences between the footprints are taken into account, which will complicate our study and be out of the main scope of this paper). Furthermore, LAS-measured H is much more stable in the daytime evolution whereas H derived from EC fluctuates seriously with time.

3.3. Remote sensing data

MODIS, onboard the TERRA satellite, has 36 spectral channels ranging from 0.405 to 14.385 μm and can acquire data at three spatial resolutions —250, 500, 1000 m. To date, 44 distinct MODIS products related to a variety of disciplines, including land surface, atmospheric sciences and oceanography, have been developed by the MODIS Science Team. MODIS data products used in this work are land surface temperature/emissivity (MOD11A1 and MOD11_L2), NDVI (MOD13A2), Calibrated Radiances (MOD021KM), Geolocation (MOD03), Precipitable Water (MOD05_L2) products. All 24 clear-sky MODIS data from May 23rd to August 21st over our study area are used to estimate the EF, ET and H using the T_s–F_r triangle method/algorithm. The overpass-time (local solar time) and view zenith angle corresponding to the 24 clear-sky MODIS data vary approximately from 10:06 to 11:30 AM and from about 5 to 60° respectively.

MOD11A1 (MODIS/Terra Land Surface Temperature/Emissivity Daily L3 Global 1 km SIN Grid) and MOD13A2 (MODIS/Terra Vegetation Indices 16-Day L3 Global 1 km SIN Grid), generated by the MODIS Adaptive Processing System (MODAPS) at the U. S. Geological Survey EROS Data Center (EDC), are stored as gridded level 3 products in the Integerized Sinusoidal projection with a nominal spatial resolution of 1 km (about 926 m) in the HDF (Hierarchical Data Format) format. Daytime surface temperature data (LST_Day_1km), daytime overpass-time (Day_view_time) and 16-day NDVI data (1_km_16_days_NDVI) extracted respectively from the MOD11A1 and MOD13A2 products are re-projected to Albers Equal Area (AEA) projection with the MRT (MODIS Reprojection Tool). The difference between MOD11_L2 and MOD11A1 is the different spatial resolutions, in which the spatial resolution of MOD11_L2 product is 1000 m same as that of the following three MODIS products.

MOD021KM, MOD03 and MOD05_L2 can be accessed from the LAADS (Level 1 and Atmosphere Archive and Distribution System) web. MOD021KM is consisted of calibrated and geolocated TOA radiances and reflectances for 36 bands. MOD03 product mainly

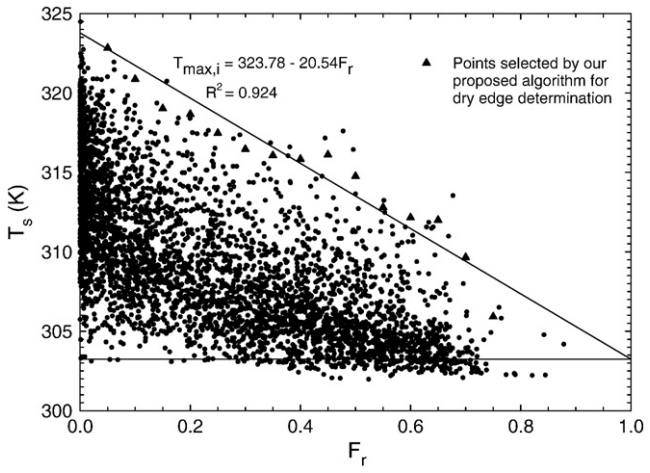

Fig. 7. A plot of T_s against F_r in the two-dimensional space for MODIS data acquired on day 201 and the corresponding dry and wet edges determined automatically by the proposed algorithm.

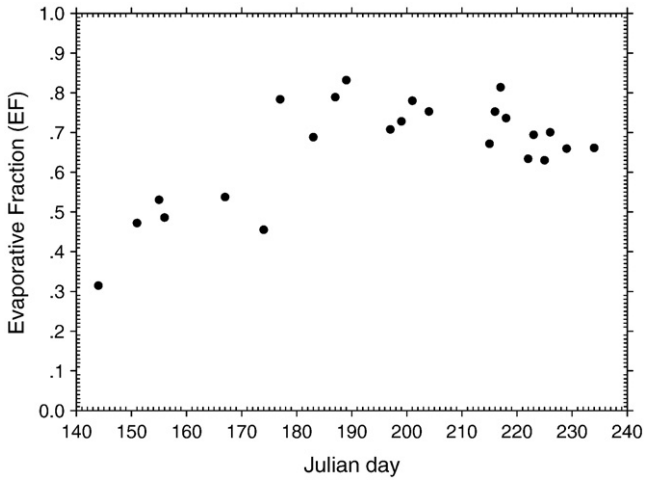

Fig. 9. Evaporative fraction of the LAS site estimated from MODIS data using the proposed algorithm for 24 clear-sky days.

includes datasets of geodetic coordinates (latitude and longitude), solar zenith and azimuth angles, satellite zenith and azimuth angles, and ground elevation for each 1-km sample (pixel). MOD05_L2 contains column water-vapor amounts over clear land areas and above clouds over both land and ocean.

3.4. Results and validation

The algorithm described in Section 2 is applied to all 24 clear-sky MODIS data acquired over our study area. As an example, Fig. 7 shows a plot of T_s against F_r in the two-dimensional space for MODIS data acquired on Julian day 201 and the corresponding dry and wet edges determined automatically by the proposed algorithm. This figure confirms that the pixels in the study area form a triangle in the two-dimensional space T_s–F_r and the dry and wet edges can be determined on the basis of the triangle space using our proposed algorithm. Similar results are obtained for other 23 clear-sky days.

Fig. 8 shows the surface net radiation (R_n), soil heat flux (G) and sensible heat flux (H) estimated from MODIS data alone on the LAS instrument site using our proposed edges determination algorithm for the T_s–F_r method for 24 clear-sky days at MODIS overpass time. From this figure, one can see that the R_n for all 24 clear-sky days varies from about 518 to 739 W/m^2 with the mean value of 618 W/m^2. The minimum and maximum R_n values occur on Julian days 226 and 177 respectively. Large variation of R_n from day to day may be due to the presence of clouds and/or due to the variations of MODIS local solar time varying from 10:06 to 11:30 AM for the 24 clear-sky days. There is no remarkable variation in the soil heat flux as F_r changes a bit from 0.02 to 0.29 during this period. The mean, minimum and maximum values of soil heat flux are 209, 172 and 248 W/m^2 respectively. In most cases, MODIS-derived sensible heat flux is smaller than the soil heat flux at the LAS site, which may be related to the relatively high surface soil water content in this area during the LAS operation period.

Fig. 9 displays EF estimated from MODIS data alone on the LAS site using our edges determination algorithm for the T_s–F_r method for 24 clear-sky days at MODIS overpass time. One can see from this figure that EF varies from 0.315 (day 144) to 0.832 (day 189) with the mean value of 0.659. EF increases rapidly from the end of May to the end of June, which is corresponding to precipitation increase during the rainfall season from June. Before June 30th, EF is generally lower than 0.55 (an exception occurs on Julian day 177) while during the period of July to August, EF varies mainly from 0.63 to 0.83. This relatively high EF during the period from the end of June to August may be due to the fact that this period is within the period of rainfall season in our study area.

Fig. 10 illustrates the highest surface temperature (T_{smax}) at the dry edge and surface temperature for the wet edge (T_{smin}, the lowest

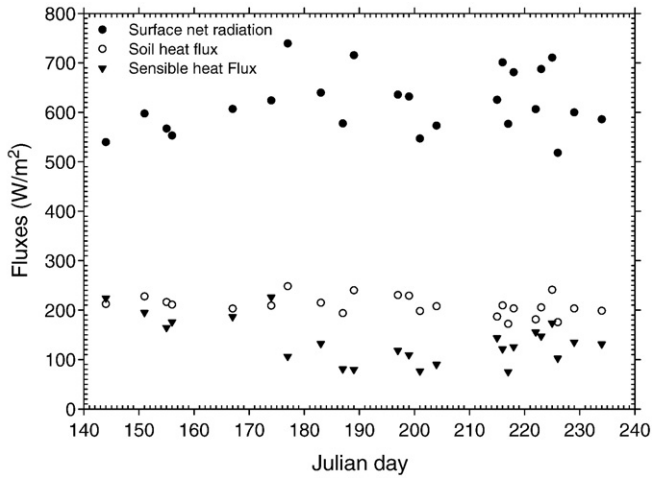

Fig. 8. Surface net radiation, soil heat flux and sensible heat flux of the LAS site derived from MODIS data using our proposed algorithm for 24 clear-sky days.

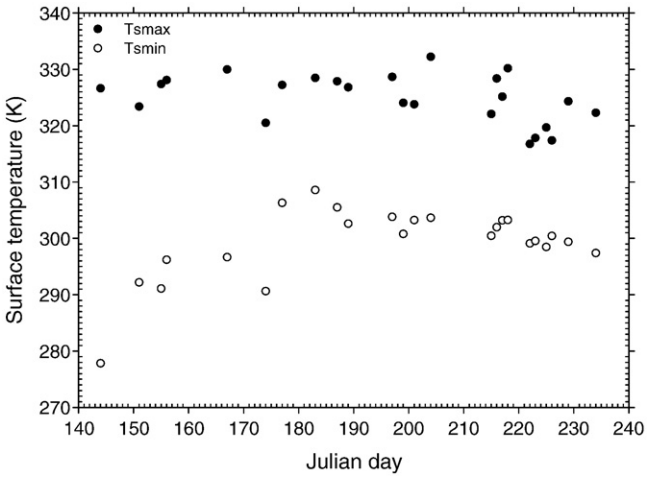

Fig. 10. The highest surface temperature at the dry edge (T_{smax}) and surface temperature at the wet edge (T_{smin}) inferred from MODIS data using our proposed algorithm for 24 clear-sky days.

Table 2
Statistics of the determined dry edges by our edges determination algorithm for 24 clear-sky days (a and b respectively represent the intercept and slope of the dry edge).

Julian day	*a*	*b*	R^2
144	326.63	−48.79	0.957
151	323.39	−31.20	0.947
155	327.38	−36.29	0.982
156	328.10	−31.88	0.918
167	329.97	−33.32	0.959
174	320.49	−29.86	0.971
177	327.22	−20.92	0.961
183	328.48	−19.90	0.922
187	327.88	−22.37	0.979
189	326.82	−24.21	0.921
197	328.65	−24.83	0.909
199	324.05	−23.25	0.829
201	323.78	−20.54	0.924
204	332.23	−28.57	0.944
215	322.08	−21.62	0.942
216	328.38	−26.41	0.932
217	325.16	−21.95	0.894
218	330.18	−26.91	0.951
222	316.76	−17.66	0.938
223	317.82	−18.27	0.929
225	319.68	−21.20	0.955
226	317.38	−16.93	0.921
229	324.32	−24.92	0.941
234	322.30	−24.90	0.947

surface temperature at the dry edge) obtained using our edges determination algorithm for 24 clear-sky days at MODIS overpass time. These surface temperatures are deduced from the determined dry edges for the 24 T_s–F_r triangles. T_{smax} varies from 316.8 (Julian day 222) to 332.2 K (Julian day 204) and T_{smin} from 277.8 (Julian day 144) to 308.6 K (Julian day 183). It should be noted that range of fractional vegetation cover as large as possible is of crucial importance for the determination of dry and wet edges in our work, which gives a possible explanation to the relatively low T_{smin} on Julian day 144 over the study area since the variation of F_r is only from 0 to 0.4. R^2 for the linear fit of the dry edge in all 24 constructed T_s–F_r triangles ranges from 0.829 to 0.982 (see Table 2), implying that Eq. (3) can well depict the relationship between T_s and F_r in the dry edge.

As a validation, Fig. 11 shows a comparison of MODIS-derived *H* using the T_s–F_r triangle method with LAS-measured *H* for 24 clear-sky days during the period of LAS operation. A very good agreement can be found in this figure with RMSE = 25.07 W/m^2. MODIS-derived *H* varies from about 75.3 to 226.2 W/m^2 with the mean value of 136.7 W/m^2. Large discrepancies (ΔH) between MODIS-derived *H* and LAS-measured *H* occur on Julian days 167 ($\Delta H = 55.3$ W/m^2), 174 ($\Delta H = 67$ W/m^2), 217 ($\Delta H = -49.7$ W/m^2), and 226 ($\Delta H = -40.6$ W/m^2). On Julian days 165 and 173, heavy rainfalls took place in the study area, leading to an inaccurate determination of dry and wet edges (i.e. T_{smax} and (T_{smax}–T_{smin}) decrease), and causing probably an underestimation of EF and an overestimation of *H* on Julian days 167 and 174.

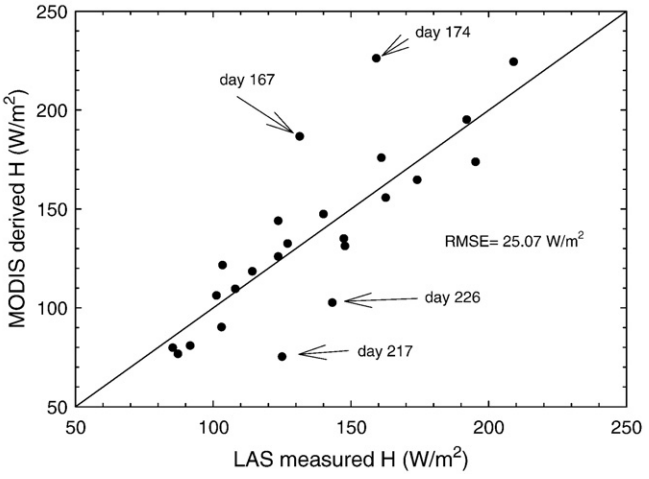

Fig. 11. Comparisons of sensible heat flux estimated from MODIS data using our proposed algorithm with that measured by LAS instrument for 24 clear-sky days.

Due to the lack of sufficient information, it is not yet possible for us to explain the possible reasons for relatively large discrepancies found on Julian days 217 and 226. It might be related to the relatively low surface net radiation ($R_n = 576$ W/m^2, 518 W/m^2 for Julian days 217 and 226 respectively) derived at MODIS overpass time on these days when compared with values estimated on Julian days 216 ($R_n = 710$ W/m^2) and 225 ($R_n = 710$ W/m^2). An advantage in the T_s–F_r triangle method is that as long as the ratio of difference between T_{si} and $T_{max,i}$ to the difference between $T_{max,i}$ and $T_{min,i}$ (see Fig. 1) does not change for a given F_r, an accurate combined-effect parameter ϕ and evaporative fraction for a given pixel (T_{si}, F_r) can be obtained, implying that the exact placements of both dry and wet edges do not affect the results significantly but their relative positions do.

Uncertainty of estimated *H* on the 24 clear-sky days comes from several sources. There are a lot of papers indicating that $\phi_{max} = 1.26$ could be used to identify the potential ET conditions (Crago & Brutsaert, 1992; Jiang & Islam, 1999; Priestley & Taylor, 1972). Combing Eqs. (2), (5) and (6), the effect of ϕ_{max} on EF estimation in the T_s–F_r triangular space can be expressed as:

$$\frac{\partial EF}{\partial \phi_{max}} = \frac{\Delta}{\Delta+\gamma}\left(\frac{T_{max,i}-T_{si}}{T_{max,i}-T_{min,i}}(1-F_r)+F_r\right) \le \frac{\Delta}{\Delta+\gamma}. \quad (15)$$

Since $\Delta/(\Delta+\gamma)$ varies from 0.55 to 0.85 for T_a ranging from 10 to 40 °C, an error of 0.1 on ϕ_{max} can only lead to an error of EF less than 0.085.

As for the effects of both $NDVI_{min}$ and $NDVI_{max}$ on F_r used in our study, they can be derived analytically from Eq. (4) as follows:

$$F_1 = \frac{\partial F_r}{\partial NDVI_{min}} = 2\frac{(NDVI-NDVI_{min})(NDVI-NDVI_{max})}{(NDVI_{max}-NDVI_{min})^3} \quad (16)$$

$$F_2 = \frac{\partial F_r}{\partial NDVI_{max}} = \frac{-2(NDVI-NDVI_{min})^2}{(NDVI_{max}-NDVI_{min})^3}. \quad (17)$$

From Eq. (16), one can see that $F_1 = 0$ if $NDVI = NDVI_{min}$ or $NDVI = NDVI_{max}$ and F_1 reaches its maximum at $NDVI = (NDVI_{max} + NDVI_{min})/2$. Inserting typical value of 0.6 for $NDVI_{max}$–$NDVI_{min}$, maximum of F_1 is equal to −0.83. Therefore, an error of 0.1 on $NDVI_{min}$ will lead to an error of F_r from −0.083 to 0.

Eq. (17) shows that $F_2 = 0$ if $NDVI = NDVI_{min}$ and F_2 reaches its maximum at $NDVI = NDVI_{max}$. Inserting typical value of 0.6 for $NDVI_{max}$–$NDVI_{min}$, maximum of F_2 is equal to −3. Therefore, an error of 0.1 on $NDVI_{max}$ will lead to an error of F_r from −0.3 to 0. Fortunately, F_r is closed to 1 when NDVI approaches to its maximum value ($NDVI_{max}$). Under such circumstance, EF is also closed to 1, implying that no large error on EF and ET can be produced by the change of $NDVI_{max}$.

The impact of uncertainty of F_r on (R_n–G) in our study can be also derived analytically from Eq. (11) and can be written as:

$$\frac{\partial(R_n-G)}{\partial F_r} = \frac{\partial(R_n - R_n(\Gamma_v + (1-F_r)(\Gamma_s-\Gamma_v)))}{\partial F_r} = (\Gamma_s-\Gamma_v)R_n. \quad (18)$$

From this equation, one can note that (R_n–G) will change by about $0.035R_n$ if F_r changes 0.1, namely an error of 0.1 on F_r will lead to an

error of (R_n–G) varying from 3.5 to 28 W/m^2 for R_n ranging from 100 to 800 W/m^2.

It should be also emphasized that uncertainties in the sensible heat flux derived from T_s–F_r triangle are partly attributed to the uncertainty related to the estimation of both R_n and G. Tang et al. (2006) reported the RMSE of less than 20 W/m^2 for clear-sky days by comparing the estimated surface net shortwave radiation with MODIS products with in-situ measured values at YuCheng field site during an extended period of time covering all seasons in 2003. A comparison of estimated surface net longwave radiation from Tang and Li (2008) with field measurements at six sites of the Surface Radiation Budget Network in United States has shown a RMSE of approximately 26 W/m^2 at MODIS overpass time of cloud-free days in 2006. As G accounts for a large portion of R_n over our study area, it will have large influences on the uncertainties of the estimated sensible and latent heat fluxes. Noting that comparisons of estimated EF with ground-based measurements are essentially the true validation of the T_s–VI triangle method for ET estimates because EF is a fairly conservative quantity over the course of a single day or from one day to the next and is much more informative than ET. Unfortunately, as there were no instruments equipped to measure R_n, G and EF from May to August at our LAS site and meteorological stations, there were no in-situ measurements of R_n G and EF available at the grassland. Therefore, it is impossible to further investigate the sources of uncertainties in sensible and latent heat fluxes.

4. Conclusions

A practical algorithm was developed for quantitative determination of dry and wet edges for the T_s–VI triangle method from MODIS data and products. This algorithm can provide an estimation of surface net radiation, soil heat flux, evaporative fraction and evapotranspiration at regional scale from MODIS data and products alone.

Determination of dry and wet wedges in T_s–VI triangular space generally involves a large degree of uncertainty. If the surface soil volumetric water content ranges from 0 to 1 for all given fractional vegetation covers, the observed wet edge can be treated as the true wet edge with potential ET and can be probably determined in an analytical way. However, this cannot be easily realized in arid and semi-arid areas because it is hard to find potentially evaporating pixels in these climate regions. The range of F_r depends on the growth stage of vegetation and the spatial representativeness of selected study area. The rules and algorithm proposed in this paper give a feasible way to estimate the highest surface temperature at each F_r interval and subsequently determine the dry and wet edges in arid and semi-arid climate regions from the T_s–F_r triangular space. Although assumption of two-step linear interpolation scheme involved in the estimation of the combined-effect parameter ϕ and EF is still questionable and not yet verified directly, a very good agreement is found with the RMSE = 25.07 W/m^2 when sensible heat flux estimated from MODIS data is compared with that measured by LAS instrument. The uncertainty of LAS-measured H from uncertainties of meteorological/surface measurements, Bowen ratio and LAS measurements is evaluated to be about 9.2 W/m^2 in our study cases.

Problems encountered in the determination of dry and wet edges during the period of our experiment mainly include: (1) only few points that were not contaminated by cloud in the T_s–VI space can be obtained on partly cloudy days in the study area, which will make the T_s–VI triangle method for ET estimates unreliable; and (2) in a short period after a rainfall event, the observed dry edge in the T_s–VI triangle may not indicate pixels with minimum ET for the given F_r due to the non-zero surface soil water content. If the observed dry edge is regarded to represent the true dry edge in this case, uncertainty and error will occur. Fortunately, wet surface soil will soon become dry as a result of large potential ET in the arid and semi-arid areas on a clear day.

Analytical analysis shows that an error of 0.1 on F_r will lead to an error of 0.035R_n on the estimation of surface available energy used in this paper and the effect of ϕ_{max} on EF estimation in the T_s–F_r triangular space is very small, an error of 0.1 on ϕ_{max} can only lead to an error of EF less than 0.085. Moreover, the effects of both $NDVI_{min}$ and $NDVI_{max}$ on F_r for a given NDVI depend on the NDVI itself, an error of 0.1 on $NDVI_{min}$ and $NDVI_{max}$ will lead to an error of F_r respectively from −0.083 to 0 and −0.3 to 0. Fortunately, when NDVI approaches $NDVI_{max}$, EF also approaches 1, implying that no large error on EF and ET can be generated by an error on $NDVI_{max}$.

To reduce the uncertainty in the estimation of turbulent heat fluxes from the T_s–F_r method, further work needs to be carried out to verify the relevant parameters/variables step by step provided that data required are available in the future and more validation work needs to be performed in other different regions for the proposed algorithm. In addition, further work needs also to be carried out to explore the non-linearity of EF (ϕ) in the T_s–VI triangular space for a given atmospheric forcing and the use of a scaled temperature T^* (varying from 0 to 1.0) instead of the use of absolute T_s to construct the scaled surface temperature–vegetation index (for example, T^*–F_r) triangle.

Acknowledgements

The authors would like to thank the four anonymous reviewers for their valuable comments that have greatly improved this paper. This work was partly supported by the National Natural Science Foundation of China under Grant 40871169, by the State Key Laboratory of Resource and Environment Information System under Grant 088RA400SA and by the Knowledge Innovation Project (KSCX2-YW-N-003) of the Chinese Academy of Sciences. Mr. R. Tang is financially supported by China Scholarship Council for his stay in LSIIT, France.

References

Allen, R. G., Tasumi, M., & Trezza, R. (2007). Satellite-based energy balance for mapping evapotranspiration with internalized calibration (METRIC)-model. *Journal of Irrigation and Drainage Engineering*, *133*, 380−394.

Asanuma, J., & Iemoto, K. (2007). Measurements of regional sensible heat flux over Mongolian grassland using Large Aperture Scintillometer. *Journal of Hydrology*, *333*, 58−67.

Bastiaanssen, W. G. M. (2000). SEBAL-based sensible and latent heat fluxes in the irrigated Gediz Basin, Turkey. *Journal of Hydrology*, *229*, 87−100.

Batra, N., Islam, S., Venturini, V., Bisht, G., & Jiang, L. (2006). Estimation and comparison of evapotranspiration from MODIS and AVHRR sensors for clear sky days over the Southern Great Plains. *Remote Sensing of Environment*, *103*, 1−15.

Boni, G., Entekhabi, D., & Castelli, F. (2001). Land data assimilation with satellite measurements for the estimation of surface energy balance components and surface control on evaporation. *Water Resources Research*, *37*, 1713−1722.

Carlson, T. N., Gillies, R. R., & Schmugge, T. J. (1995). An interpretation of methodologies for indirect measurement of soil water content. *Agricultural and Forest Meteorology*, *77*, 191−205.

Carlson, T., & Ripley, D. (1997). On the relation between NDVI, fractional vegetation cover, and leaf area index. *Remote Sensing of Environment*, *62*, 241−252.

Carlson, T. (2007). An overview of the "Triangle Method" for estimating surface evapotranspiration and soil moisture from satellite imagery. *Sensors*, *7*, 1612−1629.

Choudhury, B. J. (1989). Estimating evaporation and carbon assimilation using infrared temperature data. In: G. Asrar (Ed.), *Vistas in modeling, in theory and applications of optical remote sensing* (pp. 628−690). New York: Wiley.

Courault, D., Seguin, B., & Olioso, A. (2005). Review on estimation of evapotranspiration from remote sensing data: From empirical to numerical modeling approaches. *Irrigation and Drainage Systems*, *19*, 223−249.

Crago, R. D., & Brutsaert, W. (1992). A comparison of several evaporation equations. *Water Resources Research*, *28*, 951−954.

Daughtry, C. S. T., Kustas, W. P., Moran, M. S., Pinter, P. J. J., Jackson, R. D., Brown, P. W., et al. (1990). Spectral estimates soil heat flux of net radiation and soil heat flux. *Remote Sensing of Environment*, *32*, 111−124.

Glenn, E. P., Huete, A. R., Nagler, P. L., Hirschboeck, K. K., & Brown, P. (2007). Integrating remote sensing and ground methods to estimate evapotranspiration. *Critical Reviews in Plant Sciences*, *26*, 139−168.

Goward, S., Cruickshanks, G. D., & Hope, A. (1985). Observed relation between thermal emission and reflected spectral radiance of a complex vegetated landscape. *Remote Sensing of Environment*, *18*, 137−146.

Hassan, Q. K., Bourque, C. P. A., Meng, F. R., & Cox, R. M. (2007). A wetness index using terrain-corrected surface temperature and normalized difference vegetation index

derived from standard MODIS products: An evaluation of its use in a humid forest-dominated region of eastern Canada. *Sensors*, *7*, 2028−2048.
Hatfield, J. L. (1983). Evapotranspiration obtained from remote sensing methods. *Advances in Irrigation*, *2*, 395−416.
Jackson, R. D., Reginato, R. J., & Idso, S. B. (1977). Wheat canopy temperature: A practical tool for evaluating water requirements. *Water Resources Research*, *13*, 651−656.
Jiang, L., & Islam, S. (1999). A methodology for estimation of surface evapotranspiration over large areas using remote sensing observations. *Geophysical Research Letters*, *26*, 2773−2776.
Jiang, L., & Islam, S. (2001). Estimation of surface evaporation map over Southern Great Plains using remote sensing data. *Water Resources Research*, *37*, 329−340.
Jiang, L., & Islam, S. (2003). An intercomparison of regional latent heat flux estimation using remote sensing data. *International Journal of Remote Sensing*, *24*, 2221−2236.
Jiang, L., Islam, S., & Carlson, T. N. (2004). Uncertainties in latent heat flux measurement and estimation: Implications for using a simplified approach with remote sensing data. *Canadian Journal of Remote Sensing*, *30*, 769−787.
Jiang, L., Islam, S., Guo, W., Singh Jutla, A., Senarath, S. U. S., Ramsay, B. H., et al. (2009). A satellite-based Daily Actual Evapotranspiration estimation algorithm over South Florida. *Global and Planetary Change*, *67*, 62−77.
Kairu, E. N. (1991). A review of methods for estimating evapotranspiration particularly those that utilize remote sensing. *GeoJournal*, *25*, 371−376.
Kalma, J. D., McVicar, T. R., & McCabe, M. F. (2008). Estimating land surface evaporation: A review of methods using remotely sensed surface temperature data. *Surveys in Geophysics*, *29*, 421−469.
Kustas, W. P., & Norman, J. M. (1996). Use of remote sensing for evapotranspiration monitoring over land surfaces. *Hydrological Sciences Journal*, *41*, 495−516.
Lambin, E. F., & Ehrlich, D. (1996). The surface temperature–vegetation index space for land cover and land-cover change analysis. *International Journal of Remote Sensing*, *17*, 463−487.
Li, F. Q., & Lyons, T. J. (1999). Estimation of regional evapotranspiration through remote sensing. *Journal of Applied Meteorology*, *38*, 1644−1654.
Li, X., Ma, M. G., Wang, J., Liu, Q., Che, T., Hu, Z., et al. (2008). Simultaneous remote sensing and ground-based experiment in the Heihe river basin: Scientific objectives and experiment design.*Progress in Geography*, *23*, 897−914 (In Chinese).
Li, Z. -L., Tang, R., Wan, Z., Bi, Y., Zhou, C., Tang, B., et al. (2009). A review of current methodologies for regional evapotranspiration estimation from remotely sensed data. *Sensors*, *9*, 3801−3853.
Marx, A., Kunstmann, H., Schüttemeyer, D., & Moene, A. F. (2008). Uncertainty analysis for satellite derived sensible heat fluxes and scintillometer measurements over Savannah environment and comparison to mesoscale meteorological simulation results. *Agricultural and Forest Meteorology*, *148*, 656−667.
Moran, M. S., Clarke, T. R., Inoue, Y., & Vidal, A. (1994). Estimating crop water deficit using the relationship between surface–air temperature and spectral vegetation index. *Remote Sensing of Environment*, *49*, 246−363.
Nemani, R. R., Pierce, L., & Running, S. W. (1993). Developing satellite-derived estimates of surface moisture status. *Journal of Applied Meteorology*, *32*, 548−557.
Norman, J. M., Kustas, W. P., & Humes, K. S. (1995). A two-source approach for estimating soil and vegetation energy fluxes from observations of directional radiometric surface temperature. *Agricultural and Forest Meteorology*, *77*, 263−293.
Price, J. C. (1990). Using spatial context in satellite data to infer regional scale evapotranspiration. *IEEE Transactions on Geoscience and Remote Sensing*, *28*, 940−948.
Priestley, C. H. B., & Taylor, R. J. (1972). On the assessment of surface heat flux and evaporation using large-scale parameters. *Monthly weather review*, *100*, 81−92.
Prihodko, L., & Goward, S. N. (1997). Estimation of air temperature from remotely sensed surface observations. *Remote Sensing of Environment*, *60*, 335−346.
Stisen, S., Sandholt, I., Nørgaard, A., Fensholt, R., & Jensen, K. H. (2008). Combining the triangle method with thermal inertia to estimate regional evapotranspiration—Applied to MSG/SEVIRI data in the Senegal River basin. *Remote Sensing of Environment*, *112*, 1242−1255.
Su, Z. (2002). The surface energy balance system (SEBS) for estimation of turbulent heat fluxes. *Hydrology and Earth System Sciences*, *6*, 85−99.
Sun, D., & Kafatos, M. (2007). Note on the NDVI–LST relationship and the use of temperature-related drought indices over North America. *Geophysical Research Letters*, *34*, L24406.
Sun, Z., Wang, Q., Matsushita, B., Fukushima, T., Ouyang, Z., & Watanabe, M. (2008). A new method to define the VI–Ts diagram using subpixel vegetation and soil information: A case study over a semiarid agricultural region in the north China plain. *Sensors*, *8*, 6260−6279.
Tang, B. H., & Li, Z. -L. (2008). Estimation of instantaneous net surface longwave radiation from MODIS cloud-free data. *Remote Sensing of Environment*, *112*, 3482−3492.
Tang, B. H., Li, Z. -L., & Zhang, R. H. (2006). A direct method for estimating net surface shortwave radiation from MODIS data. *Remote Sensing of Environment*, *103*, 115−126.
Venturini, V., Bisht, G., Islam, S., & Jiang, L. (2004). Comparison of evaporative fractions estimated from AVHRR and MODIS sensors over South Florida. *Remote Sensing of Environment*, *93*, 77−86.
Wang, K., Li, Z., & Cribb, M. (2006). Estimation of evaporative fraction from a combination of day and night land surface temperatures and NDVI: A new method to determine the Priestley-Taylor parameter. *Remote Sensing of Environment*, *102*, 293−305.
Wyngaard, J. C., Izumi, Y., & Collins, S. A., Jr. (1971). Behaviour of the refractive index structure parameter near the ground. *Journal of the Optical Society of America*, *61*, 1646−1650.